Photoconductive effect on p-i-p micro-heaters integrated in silicon microring resonators

Linjie Zhou,* Haike Zhu, Heng Zhang, and Jianping Chen

State Key Laboratory of Advanced Optical Communication Systems and Networks, Department of Electronic Engineering, Shanghai Jiao Tong University, Shanghai 200240, China
*ljzhou@sjtu.edu.cn

Abstract: We study the photoconductive effect of a *p-i-p* micro-heater integrated in a microring resonator. Due to the surface state absorption (SSA) and two photon absorption (TPA) of optical wave around 1550 nm, free carriers are generated in the silicon waveguide, leading to the modulation of silicon conductivity and thus the current flowing through it. The current-voltage (I-V) response of the *p-i-p* diode is dependent on the bias voltage and can be divided into ohmic-law regime and space-charge-limited regime. The resonance peak current is more sensitive to optical power in the ohmic-law regime. Such a phenomenon can also be utilized to monitor the optical power in the waveguide.

©2014 Optical Society of America

OCIS codes: (250.5300) Photonic integrated circuits; (130.0130) Integrated optics; (230.5750) Resonators; (160.6840) Thermo-optical materials.

References and links

1. G. T. Reed and A. P. Knights, *Silicon Photonics* (Wiley Online Library, 2008).
2. R. Soref, "The past, present, and future of silicon photonics," IEEE J. Sel. Top. Quantum Electron. **12**(6), 1678–1687 (2006).
3. M. Asghari, "Silicon photonics: a low cost integration platform for datacom and telecom applications," Proc. OFC/NFOEC'2008, paper NThA4 (2008).
4. E. R. Fuchs, R. E. Kirchain, and S. Liu, "The future of silicon photonics: Not so fast? Insights from 100G ethernet LAN transceivers," J. Lightwave Technol. **29**(15), 2319–2326 (2011).
5. H. Fukuda, K. Takeda, T. Hiraki, T. Tsuchizawa, H. Nishi, R. Kou, Y. Ishikawa, K. Wada, T. Yamamoto, and K. Yamada, "Large-scale silicon photonics integrated circuits for interconnect and telecom applications," in *10th International Conference on Group IV Photonics (GFP)*, (IEEE, 2013), 130–131.
6. G. Reed, S. Mailis, M. J. Wale, and A. Willner, "Introduction to the issue on optical modulators—Technologies and applications," IEEE J. Sel. Top. Quantum Electron. **19**, 1–3 (2013).
7. D. J. Thomson, F. Y. Gardes, J.-M. Fedeli, S. Zlatanovic, Y. Hu, B. P. P. Kuo, E. Myslivets, N. Alic, S. Radic, G. Z. Mashanovich, and G. T. Reed, "50-Gb/s silicon optical modulator," IEEE Photon. Technol. Lett. **24**(4), 234–236 (2012).
8. X. Xiao, X. Li, H. Xu, Y. Hu, K. Xiong, Z. Li, T. Chu, Y. Yu, and J. Yu, "44Gbit/s Silicon Microring Modulators based on Zigzag PN Junctions," IEEE Photon. Technol. Lett. **24**(19), 1712–1714 (2012).
9. L. Zhou and A. W. Poon, "Silicon electro-optic modulators using p-i-n diodes embedded 10-micron-diameter microdisk resonators," Opt. Express **14**(15), 6851–6857 (2006).
10. L. Lu, L. Zhou, X. Sun, J. Xie, Z. Zou, H. Zhu, X. Li, and J. Chen, "CMOS-compatible temperature-independent tunable silicon optical lattice filters," Opt. Express **21**(8), 9447–9456 (2013).
11. N.-N. Feng, P. Dong, D. Feng, W. Qian, H. Liang, D. C. Lee, J. B. Luff, A. Agarwal, T. Banwell, R. Menendez, P. Toliver, T. K. Woodward, and M. Asghari, "Thermally-efficient reconfigurable narrowband RF-photonic filter," Opt. Express **18**(24), 24648–24653 (2010).
12. L. Chen and Y. K. Chen, "Compact, low-loss and low-power 8×8 broadband silicon optical switch," Opt. Express **20**(17), 18977–18985 (2012).
13. J. Cardenas, M. A. Foster, N. Sherwood-Droz, C. B. Poitras, H. L. Lira, B. Zhang, A. L. Gaeta, J. B. Khurgin, P. Morton, and M. Lipson, "Wide-bandwidth continuously tunable optical delay line using silicon microring resonators," Opt. Express **18**(25), 26525–26534 (2010).
14. A. Masood, M. Pantouvaki, G. Lepage, P. Verheyen, J. Van Campenhout, P. Absil, D. Van Thourhout, and W. Bogaerts, "Comparison of heater architectures for thermal control of silicon photonic circuits," in *10th International Conference on Group IV Photonics (GFP)*, (IEEE, 2013), 83–84.

15. A. Masood, M. Pantouvaki, D. Goossens, G. Lepage, P. Verheyen, D. Van Thourhout, P. Absil, and W. Bogaerts, "CMOS-compatible tungsten heaters for silicon photonic waveguides," in *9th International Conference on Group IV Photonics (GFP)*, (IEEE, 2012), 234–236.
16. P. Dong, W. Qian, H. Liang, R. Shafiiha, N.-N. Feng, D. Feng, X. Zheng, A. V. Krishnamoorthy, and M. Asghari, "Low power and compact reconfigurable multiplexing devices based on silicon microring resonators," Opt. Express **18**(10), 9852–9858 (2010).
17. C. Li, J. H. Song, J. Zhang, H. Zhang, S. Chen, M. Yu, and G. Q. Lo, "Silicon polarization independent microring resonator-based optical tunable filter circuit with fiber assembly," Opt. Express **19**(16), 15429–15437 (2011).
18. L. Zhou, X. Zhang, L. Lu, and J. Chen, "Tunable vernier microring optical filters with p-i-p type microheaters," IEEE Photon. J. **5**(4), 6601211 (2013).
19. M. Casalino, G. Coppola, M. Iodice, I. Rendina, and L. Sirleto, "Near-infrared sub-bandgap all-silicon photodetectors: state of the art and perspectives," Sensors (Basel) **10**(12), 10571–10600 (2010).
20. H. Chen, X. Luo, and A. W. Poon, "Cavity-enhanced photocurrent generation by 1.55 μm wavelengths linear absorption in a pin diode embedded silicon microring resonator," Appl. Phys. Lett. **95**(17), 171111 (2009).
21. H. Yu, D. Korn, M. Pantouvaki, J. Van Campenhout, K. Komorowska, P. Verheyen, G. Lepage, P. Absil, D. Hillerkuss, L. Alloatti, J. Leuthold, R. Baets, and W. Bogaerts, "Using carrier-depletion silicon modulators for optical power monitoring," Opt. Lett. **37**(22), 4681–4683 (2012).
22. H. Chen and A. W. Poon, "Two-photon absorption photocurrent in pin diode embedded silicon microdisk resonators," Appl. Phys. Lett. **96**(19), 191106 (2010).
23. H. Zhu, L. Zhou, X. Sun, J. Xie, Z. Zou, L. Lu, X. Li, and J. Chen, "Photocurrent generation in a silicon waveguide integrated with periodically interleaved pn junctions," in *Conference on Lasers and Electro-Optics Pacific Rim (CLEO-PR)* (IEEE, 2013)
24. S. M. Sze and K. K. Ng, *Physics of Semiconductor Devices* (Wiley, 2006).
25. S. Jain, W. Geens, A. Mehra, V. Kumar, T. Aernouts, J. Poortmans, R. Mertens, and M. Willander, "Injection- and space charge limited-currents in doped conducting organic materials," J. Appl. Phys. **89**(7), 3804–3810 (2001).
26. A. Grinberg and S. Luryi, "Space-charge-limited current and capacitance in double-junction diodes," J. Appl. Phys. **61**(3), 1181–1189 (1987).
27. N. Harrick, "Optical spectrum of the semiconductor surface states from frustrated total internal reflections," Phys. Rev. **125**(4), 1165–1170 (1962).
28. G. Samoggia, A. Nucciotti, and G. Chiarotti, "Optical detection of surface states in Ge," Phys. Rev. **144**(2), 749–751 (1966).
29. F. Allen and G. Gobeli, "Work function, photoelectric threshold, and surface states of atomically clean silicon," Phys. Rev. **127**(1), 150–158 (1962).
30. V. Bortolani, C. Calandra, and A. Sghedoni, "Surface states in Si," Phys. Lett. A **34**(3), 193–194 (1971).
31. G. Chiarotti, S. Nannarone, R. Pastore, and P. Chiaradia, "Optical absorption of surface states in ultrahigh vacuum cleaved (111) surfaces of Ge and Si," Phys. Rev. B **4**(10), 3398–3402 (1971).
32. T. Baehr-Jones, M. Hochberg, and A. Scherer, "Photodetection in silicon beyond the band edge with surface states," Opt. Express **16**(3), 1659–1668 (2008).
33. H. K. Tsang and Y. Liu, "Nonlinear optical properties of silicon waveguides," Semicond. Sci. Technol. **23**(6), 064007 (2008).
34. A. C. Turner-Foster, M. A. Foster, J. S. Levy, C. B. Poitras, R. Salem, A. L. Gaeta, and M. Lipson, "Ultrashort free-carrier lifetime in low-loss silicon nanowaveguides," Opt. Express **18**(4), 3582–3591 (2010).
35. J. Heebner, R. Grover, T. Ibrahim, and T. A. Ibrahim, *Optical Microresonators: Theory, Fabrication, and Applications* (Springer, 2008, Chap. 3).
36. M. Notomi, A. Shinya, S. Mitsugi, G. Kira, E. Kuramochi, and T. Tanabe, "Optical bistable switching action of Si high-Q photonic-crystal nanocavities," Opt. Express **13**(7), 2678–2687 (2005).

1. Introduction

Silicon photonics provides the solution for compact and low-cost optical components compatible with complementary metal-oxide-semiconductor (CMOS) circuitry [1, 2]. Multiple basic optical functions have been demonstrated on silicon-on-insulator substrate in recent years, making a great impact on telecom and datacom [3–5]. Silicon has an indirect bandgap of 1.12 eV, making it transparent in the telecom wavelength around 1.31 and 1.55 μm. Silicon can make low-loss optical waveguides and versatile passive devices. To make these devices tunable or reconfigurable, active tuning elements have to be integrated with them. The two basic mechanisms that are commonly used to change the refractive index of silicon are based on the free-carrier plasma dispersion (FCD) effect and thermo-optic (TO) effect. The former one has a relatively fast tuning speed yet the tuning range is limited by the accompanied free-carrier absorption (FCA) loss. It is routinely used in the form of *p-n* or *p-i-*

n diode for high-speed silicon optical modulators [6–9]. The latter one, on the other hand, has slow response but the tuning range is relatively large due to the large TO coefficient of silicon, making it suitable for devices where high speed response is not a must, like filters [10, 11], switches [12], delay lines [13] *etc*. To make a micro-heater compatible with CMOS fabrication techniques, the selectable materials are basically limited to three types: metal, silicide, and silicon [14]. Metal has high absorption loss and hence it cannot be positioned too close to the waveguide. Heater lines are usually made of high resistivity metals like tungsten (W) [15], titanium (Ti) [11, 16], and titanium nitride (TiN) [12, 17]. Silicide is formed by the chemical reaction between silicon and metal, which is used to make good contact and improve adhesion in CMOS circuits. Heater lines made of silicide and highly doped silicon can be put beside the waveguide to reduce the interaction distance.

Recently, we reported to use a *p-i-p* diode to tune the microring filter, where the generated heat has intimate contact with the silicon waveguide in favor of thermal tuning [18]. In fact, the *p-i-p* diode exhibits double-junction features, distinct from a simple resistor. As the silicon waveguide composes the quasi-intrinsic region of the *p-i-p* diode, free carriers generated by photon absorption can modify the electrical behavior of the diode, which in turn affects the thermal effect. Surface state absorption (SSA) and defect-enabled mid-bandgap absorption (MBA) are the linear photon absorption mechanisms commonly employed for all-silicon near-infrared optical detection [19]. Besides that, nonlinear absorption namely two-photon absorption (TPA) also plays a significant role if the optical power is high. Compared to direct inter-band photon absorption, the photocurrent generated in silicon by the above three mechanisms is usually weak. Resonances can greatly enhance the optical power inside the cavity, which has been proved to be an effective way to amplify the weak photocurrent [20, 21].

In this paper, we investigate the photoconductive effect of the *p-i-p* diode and reveal that the current through the junction can be varied by the light propagating in it. This effect is magnified by the microring resonance. Such study is important to understand the interplay between the optical absorption and thermal heating both occurring in the *p-i-p* diode. In addition, as the current reflects the optical power in the waveguide, it can also be utilized for monitoring purpose, similar to that provided by *p-n* or *p-i-n* junctions in silicon [20–23].

2. Device structure

Figure 1(a) shows the microscope image of the microring resonator integrated with a *p-i-p* diode. The microring resonator radius is 10 μm. The separation gap between the microring and the bus waveguides is 200 nm. Grating couplers are used for input/output coupling. Figure 1(b) illustrates the schematic cross-section of the *p-i-p* diode. The silicon waveguide width is 450 nm and height 220 nm. The etched depth of the waveguide is 160 nm with a 60 nm slab left to form the lateral *p-i-p* diode. The two 3-μm-wide *p*-type doped regions have a doping concentration of 10^{20} cm^{-3}, separated from the waveguide edges by 0.6 μm. The aluminum metal connection wires have ohmic contact with the two highly doped regions. The silicon waveguide has a light *p*-type doping of 10^{15} cm^{-3} from the original silicon-on-insulator (SOI) wafer. The divacancies and interstitial defect densities are low in the waveguide region, and thus the MBA effect can be neglected in the *p-i-p* diode. In our design, the *p*-type doping is wrapped around the entire microring resonator including the waveguide coupling regions, and therefore, there is photoconductive effect even at off-resonance when no light is coupled into the ring resonator.

The device was fabricated using deep ultra-violet (DUV) photolithography and plasma dry etch, resulting in waveguide sidewall root-mean-square roughness of a few nm's. The rough sidewalls cause waveguide scattering loss, but on the other side, also provide more surface states in favor of photon absorption. It should be noted that due to the discontinuity of material permittivity, the electric field is considerably enhanced near the vertical surface for

#202108 - $15.00 USD Received 27 Nov 2013; revised 12 Jan 2014; accepted 16 Jan 2014; published 24 Jan 2014
(C) 2014 OSA

transverse-electric (TE) polarization mode. The maximum of the mode intensity locates exactly at the waveguide sidewalls.

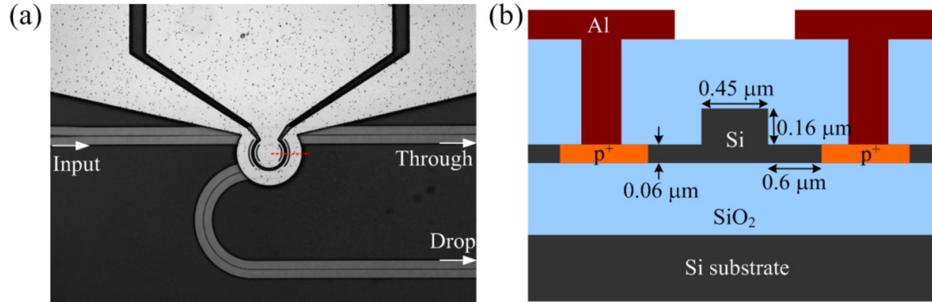

Fig. 1. (a) Optical microscope image of the fabricated *p-i-p* diode embedded microring resonator. (b) Schematic cross-section of the *p-i-p* diode. The critical dimensions are labeled.

3. Theoretical analysis

The *p-i-p* diode has two junctions, with left side being *p-i* junction and right side *i-p* junction. Unlike *p-n-p* bipolar transistor where the two depletion regions are separated by the central *n*-type base region [24], the junctions in the *p-i-p* diode can be easily punched through with a small bias due to the hole injection in the base. The holes in the base region are composed of two parts: background doping and external injection. The current-voltage (I-V) characteristic of the *p-i-p* diode is dependent on the bias level and can be divided into two regimes. In the low-bias limit, the injected hole concentration is much lower than the background intrinsic doping. In this case, the barrier height at the left *p-i* junction remains almost unchanged and the *p-i-p* diode works as a resistor. Its I-V curve obeys Ohm's law to have linear dependence. In the high-bias limit, the behavior of the I-V curve is quite different. Once the bias is high enough such that the injected holes exceed the background density, the space-charge-limited current applies. In this case, there is a large current through the *p-i-p* diode and the current density is given by the Mott-Gurney law [24]:

$$J = \frac{9}{8}\varepsilon_{si}\varepsilon_0\mu\frac{V^2}{W^3} \tag{1}$$

where V is the bias voltage, W is the width of the quasi-intrinsic region, μ is the mobility of hole, ε_{si} is the dielectric constant of silicon, and ε_0 is the permittivity in vacuum. It can be seen that in this regime the current has a quadratic dependence on voltage. The transition between the linear and parabolic regimes occurs at a threshold voltage given by [25]

$$V_{th} = \frac{8qp_0W^2}{9\varepsilon_{si}\varepsilon_0} \tag{2}$$

where q is the electric charge, p_0 is the background doping concentration. Substituting the device parameters into the above equation, we get $V_{th} \approx 3.7$ V for our *p-i-p* diode.

Figures 2(a) and 2(b) show the energy band diagrams of the *p-i-p* diode at 1V and 8V, respectively. The simulation is based on the two-dimensional simulation package, ATLAS from SILVACO. It simulates the electrical characteristics of semiconductor devices by solving the Poisson's and charge continuity equations for electrons and holes. In our simulation, the device parameters are the same with our fabricated device. The bias voltage is applied to the left electrode with respective to the right. The base region is floating. It can be seen that the potential is mostly dropped on the right *i-p* junction. There is a barrier for holes at the left *p-i* junction, which is formed entirely by the mobile holes injected into the base

#202108 - $15.00 USD Received 27 Nov 2013; revised 12 Jan 2014; accepted 16 Jan 2014; published 24 Jan 2014
(C) 2014 OSA

region [26]. The increase in bias voltage both lowers the barrier and moves its position towards the left contact (emitter). The electric field is relatively flat in the base region at low bias, while it increases dramatically in the vicinity of right junction at high bias as seen from Fig. 2(c). The rise of electric field originates from the accumulation of space charges in the base.

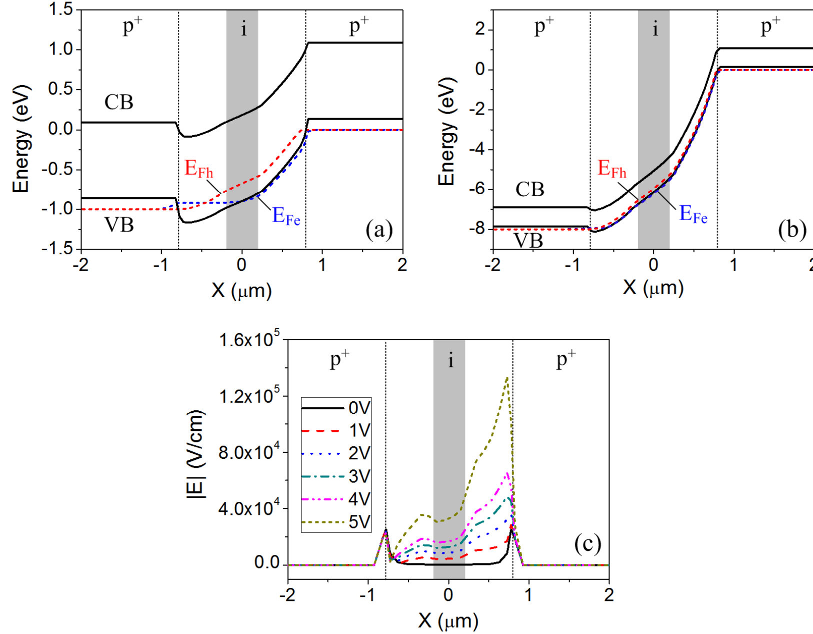

Fig. 2. (a) and (b) Energy-band diagrams along the *p-i-p* diode at (a) 1V and (b) 8V biases. (c) Electric field distribution in the *p-i-p* diode at various biases.

Due to the presence of the SSA and TPA effects, the I-V characteristics can be modified by the optical power in the *p-i-p* diode. At the low optical power level, the SSA takes the leading role. The SSA effect originates from the electronic surface states in the forbidden band gap of silicon. Because of these surface states, the optical absorption on the silicon waveguide surface extends to energies lower than the band edge [27, 28]. As a consequence, light traveling in a sub-micrometer silicon waveguide is partially absorbed and converted to free-carriers at the waveguide surface. Surface states are located within the first three or four atomic layers from the surface. At the surface, there are several transition processes, including the transition between bands of surface states in the silicon band gap, transition from the silicon valence band to an empty surface state band in the gap, transition from a filled surface state band in the gap to empty silicon conduction band [19]. Theoretical calculations and optical measurements show that there exist two bands for the surface states, and the number of states per unit area is 2.6×10^{15} states/cm^2 on clean silicon surfaces [29, 30]. With the increase in optical power, the TPA takes effect, which scales with the square of light intensity. The free carrier generation rate due to SSA and TPA can be expressed as

$$G_{opt} = \left(\alpha_{SSA} \frac{P}{A_{eff}} + \frac{1}{2} \beta_{TPA} \frac{P^2}{A_{eff}^2} \right) \frac{\lambda}{hc} \tag{3}$$

Where α_{SSA} and β_{TPA} are the SSA and TPA coefficients respectively, P is the optical power in the ring waveguide, A_{eff} is the waveguide effective area, λ is the wavelength of light in vacuum, h is the Planck's constant, and c is the speed of light in vacuum. Here we can assume

#202108 - $15.00 USD Received 27 Nov 2013; revised 12 Jan 2014; accepted 16 Jan 2014; published 24 Jan 2014
(C) 2014 OSA

the optical power in the ring waveguide is constant since the absorbed optical power only accounts for a small part. Chiarotti *et al.* measured the optical absorption due to surface state [31]. The maximum absorption occurs for photon energy between 0.4 and 0.5 eV. At 1.55 um wavelength, the absorption constant in silicon is ~5 × 10^{-3} for a two dimensional structure. The SSA coefficient α_{SSA} is 0.18 cm^{-1}, estimated from responsivity measurement [32]. The reported silicon TPA coefficient β_{TPA} in literature has an averaged value of about 0.6 cm/GW [33]. At steady state, the carrier generation rate is equal to the recombination rate, and thus the excess carrier concentration is given by

$$\Delta n = \Delta p = G_{opt}\tau \quad (4)$$

where τ is the carrier lifetime. The carrier lifetime is significantly affected by the surface recombination rate and is waveguide dimension dependent. It is in the order of ns for the sub-micrometer silicon waveguide [34]. The waveguide effective area of the fundamental TE mode is 0.12 μm^2 at 1.55 μm. From (3) and (4), the estimated excess free carrier concentration at 10 mW optical power is 3.5 × 10^{16} cm^{-3} (assuming $\tau = 3$ ns), which is mainly contributed by the SSA effect.

The generation of free carriers changes the conductivity of the base region. The conductivity is expressed as

$$\sigma = q\mu_n \Delta n + q\mu_p \left(p_0 + \Delta p\right) \quad (5)$$

where μ_n and μ_p are the electron and hole mobilities, respectively. In the linear regime, as the original hole concentration is low, photon generation has a more significant effect on the current density. On the contrary, in the parabolic regime, as injected holes (space charge) have already reached a high concentration level, photon generation has a relatively insignificant effect. It suggests the current in the *p-i-p* diode is more sensitive to optical power under a low bias.

Lastly we have to take into consideration of the microring resonance effect. The normalized through-port optical power transmission function of the microring add-drop filter can be derived from the transfer matrix approach and is given by [35]

$$T = \frac{t_2^2 a^2 - 2t_1 t_2 a\cos\phi + t_1^2}{1 - 2t_1 t_2 a\cos\phi + \left(t_1 t_2 a\right)^2} \quad (6)$$

where t_1 and t_2 are the field transmission coefficients of the input and output couplers respectively, a is the loss factor of the resonator, and ϕ is the light one-round trip phase change in the resonator. In our device the coupling is symmetric, *i.e.*, $t_1 = t_2 = t$. On resonance high optical power is built-up inside the resonator, which magnifies the photoconductive effect in the *p-i-p* diode. The build-up factor, defined as the optical power ratio between the resonator and the input waveguide, is given by

$$B = \frac{\left(1 - t^2\right) t^2 a^2}{1 - 2t^2 a\cos\phi + \left(t^2 a\right)^2} \quad (7)$$

4. Experiment

We first measure the TE-polarized transmission spectrum of the microring resonator as shown in Fig. 3(a). No bias is applied on the *p-i-p* diode. The background transmission envelop is caused by the grating couplers. The resonance free spectral range (FSR) is 9.6 nm, the quality factor is $Q \approx 10^4$, and the extinction ratio is 21 dB. From curve fitting to the measured spectrum using Eq. (6) as shown in Fig. 3(b), we get $t = 0.97$ and $a = 0.996$ (corresponding to

#202108 - $15.00 USD Received 27 Nov 2013; revised 12 Jan 2014; accepted 16 Jan 2014; published 24 Jan 2014
(C) 2014 OSA

~5.5 dB/cm waveguide loss). The inset of Fig. 3(b) shows the build-up factor versus wavelength. It reaches the maximum of 14 on resonance.

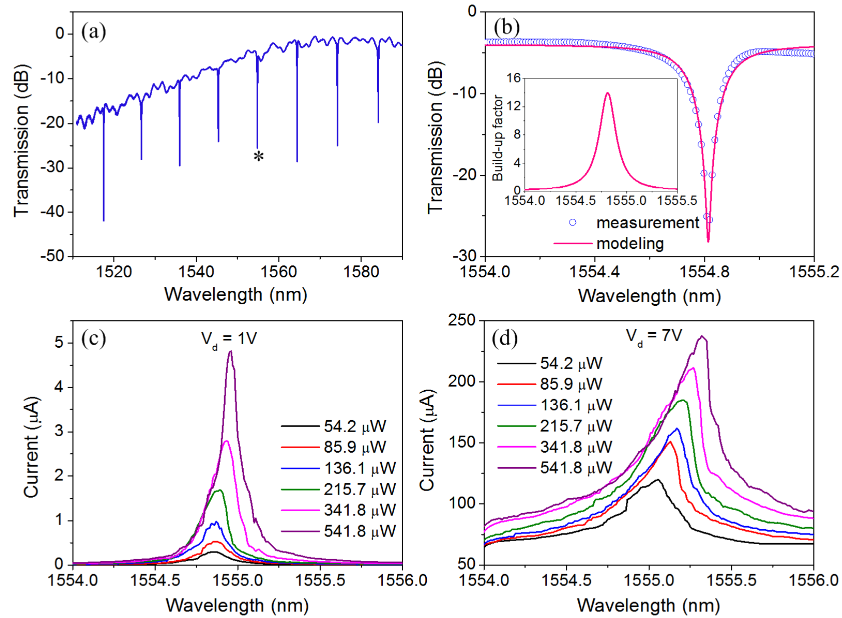

Fig. 3. (a) Measured transmission spectrum of the microring resonator. (b) Fitting of the resonance spectrum with theoretical modeling. (c) and (d) Measured current as a function of wavelength at various optical power levels. The bias voltage V_d is 1V in (c) and 7 V in (d).

Next, we measure the current as a function of wavelength around 1554.8 nm resonance for various optical powers at 1V bias as shown in Fig. 3(c). The power value refers to the estimated coupled power in the bus waveguide by subtracting the grating coupling loss from the input fiber power. It can be seen that the current is considerably increased near resonance wavelength. The increment is more pronounced when the optical power is high. The peak wavelength slightly redshifts with the increasing optical power, indicating more heat is generated inside the microring resonator. Figure 3(d) shows the current as a function of wavelength when the bias voltage is leveled up to 7 V. Compared to the low-bias case, the measured current is much higher at both off- and on-resonance wavelengths. Two observations can be made with regard to the current peak: first, the peak becomes asymmetric inclining towards the longer wavelength side; second, the peak is also broadened. For example, the full-width-half-maximum (FWHM) of the peak is ~0.13 nm at 1 V bias and 541.8 µW optical power, while it increases to ~0.35 nm at 7 V with the same power level. The asymmetric current peak comes from the modulation of silicon resistance by the optical power in the ring waveguide. Due to SSA and TPA effects, free carriers are generated by optical wave. The free carrier concentration and thus silicon conductivity is proportional to the optical power level. Hence, higher intra-cavity optical power near resonance results in a lower resistance of the silicon waveguide. According to the ohm's law, more heat is generated under a constant voltage, which in turn leads to a further redshift of the resonance. As a consequence, the current peak is skewed towards the longer wavelength side, similar to the thermal nonlinear effect observed in passive resonators [36]. Such an effect is useful for bitable and logic switch. With external thermal feeding using our *p-i-p* diode, the required optical power to generate the thermal nonlinearity is reduced, as evident from the comparison of Figs. 3(c) and 3(d).

#202108 - $15.00 USD Received 27 Nov 2013; revised 12 Jan 2014; accepted 16 Jan 2014; published 24 Jan 2014
(C) 2014 OSA

To more clearly show the dependence of the resonance-enhanced current on bias voltage, we also measure the current as a function of wavelength at other bias voltages. The extracted peak wavelength and current values (off- and on-resonances) are shown in Fig. 4. The peak wavelength red-shifts with the increasing optical power (more significant at high bias). It can be noticed that the wavelength curves for 1 V and 3V are almost overlapped, implying the heat generation is at the same level independent of the bias. There are two mechanisms for heat generation inside the microring resonator. The first one is optical heating as photons are partially absorbed by the silicon waveguide raising the temperature; the second one is resistive heating when current flows through the silicon waveguide. As discussed above, higher optical power results in a lower resistance due to the photoconductive effect. Therefore, heating from both mechanisms increases with optical power. Figure 3(a) suggests that at low bias (<3V), optical heating exceeds resistive heating, thereby changing bias has almost no effect on overall wavelength shift. As resistive heating has quadratic dependence on bias voltage, wavelength red-shifts faster once resistive heating dominates optical heating (>3V).

Because the intra-cavity optical power is maximally enhanced on resonance, the current also reaches the maximum at the resonance wavelength. From Figs. 3(b) and 3(c), we can see that the logarithm of current value changes almost linearly with the optical power. The on-resonance current curves have a slightly larger slope. Both change rates decrease with the bias voltage. For example, the on-resonance current increases 90 times (from 0.1 μA to 9 μA) when the optical power increases from 34.2 μW to 859 μW at 1 V. In contrast, the current increment is reduced to 1.7 times (from 277 μA to 476 μA) at 9 V. It indicates that such photoconductive current is more sensitive to optical power at low bias. The photogenerated free carriers change the base conductivity considerably if the *p-i-p* diode works in the ohmic-law regime. According to the theoretical analysis in the previous section, the conductivity of the base region is linearly proportional to the optical power. In the measurement range, the conductivity should increases 22 times according to the theoretical model. It lies in between the measured values at 1V (90 times) and 3V (16 times). The discrepancy at the low voltage is probably because of the weak junction feature of the *p-i-p* diode in the ohmic-law regime. It tends to behave like a phototransistor rather than a pure resistor to provide some current gain. The current increment rate reduces at the high voltage as the space-charge-limited current gradually dominates.

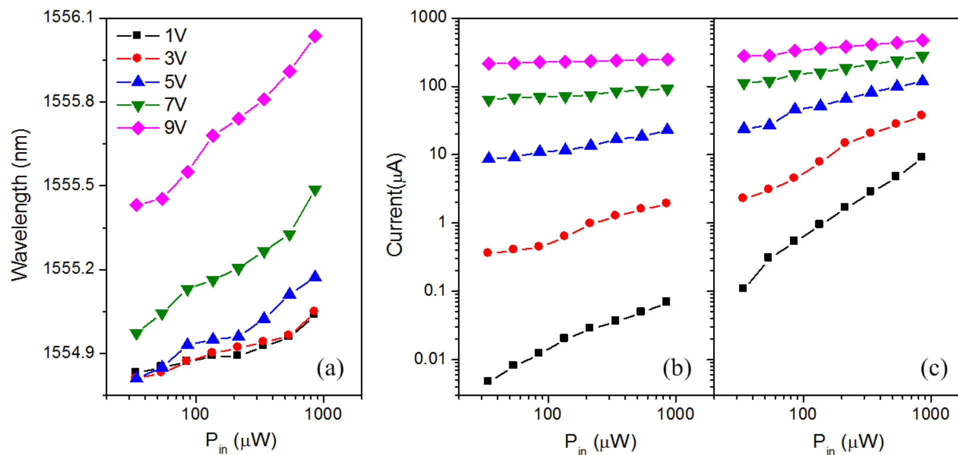

Fig. 4. (a) Current peak wavelength versus waveguide coupled optical power for various bias voltages. (b) and (c) Measured photoconductive current versus optical power. (b) is at the off-resonance (1554 nm) wavelength, and (c) is at the on-resonance (current peak) wavelength.

#202108 - $15.00 USD Received 27 Nov 2013; revised 12 Jan 2014; accepted 16 Jan 2014; published 24 Jan 2014
(C) 2014 OSA

Figure 5 shows the measured peak current changes nonlinearly with the bias voltage. After the bias exceeds a certain value (approximately 4 V), current changes more rapidly with voltage as it enters the space-charge-limited regime. Although the current is high in this regime, the optical power has less effect compared to the low-bias ohmic-law regime in terms of current increment ratio. The peak current can be an indication of the resonance optical power the microring resonator, which can be utilized for optical monitors as one application.

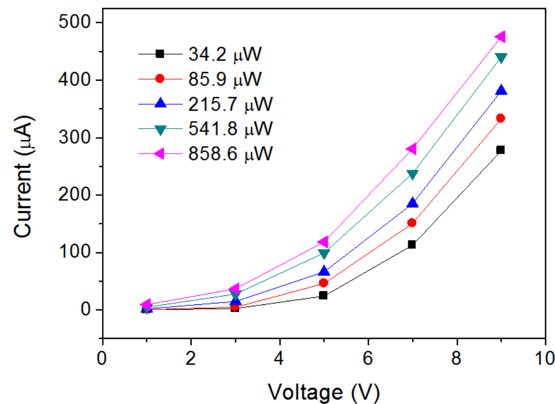

Fig. 5. Peak current-voltage curves of the *p-i-p* diode for various optical power levels.

5. Conclusion

We theoretically analyzed and experimentally explored the I-V characteristics of a *p-i-p* diode embedded in a microring resonator. Optical power in the resonator has a great impact on the I-V curve. The increment of current in response to the optical power is dependent on the bias voltage, being more significant towards the low-bias end. This study is important to understand the basic operation of a *p-i-p* micro-heater when optical wave is transmitted through. In addition, the high sensitivity of the low-bias current to optical power together with the wavelength selectivity of the microring resonator can be used to monitor a particular wavelength channel in the bus waveguide.

Acknowledgment

This work was supported in part by the 973 program (ID2011CB301700), the 863 program (2013AA014402), the National Natural Science Foundation of China (NSFC) (61007039, 61001074, 61127016, 61107041), the Science and Technology Commission of Shanghai Municipality (STCSM) Project (12XD1406400). We also acknowledge IME Singapore for device fabrication.

#202108 - $15.00 USD Received 27 Nov 2013; revised 12 Jan 2014; accepted 16 Jan 2014; published 24 Jan 2014

(C) 2014 OSA